High-Performance Bifacial Perovskite/Silicon Double-Tandem Solar Cell

Hassan Imran ⓘD, Imranzeb Durrani ⓘD, Muhammad Kamran, Tarek Mohammed Abdolkader ⓘD, *Member, IEEE*, Muhammad Faryad, and Nauman Zafar Butt ⓘD, *Member, IEEE*

Abstract*—Bifacial technology aims to boost power conversion efficiency of solar cells by effectively harvesting the albedo sunlight reflected from the earth, which is typically uncollected in conventional solar cells. We propose an innovative three-terminal (3-T), four-junction perovskite/silicon bifacial tandem solar cell that leverages albedo to surpass the theoretical limits of the traditional monofacial tandem structures. The cell stacks two identical series-connected double-junction perovskite/silicon tandem cells with a common (middle) terminal such that the bottom tandem cell is integrated upside down to effectively harvest albedo. The albedo absorption in the bottom tandem cell linearly enhances the short-circuit current of the double-tandem structure; hence, it overcomes the classical current-matching limit in series-connected tandem solar cells. We use self-consistent optical/device simulations to investigate the design optimizations of the cell and compare its performance with a conventional tandem structure. With an optimal design, the cell exhibits a remarkable efficiency of 30%–36% (bifacial gain of 10%–30%) for the albedo range of 15%–45%. The 3-T cell design works optimally for any range of albedo that is in contrast with 2-T series-connected cell for which the optimal top cell thickness changes with the value of albedo. Moreover, the proposed cell is relatively less sensitive to the process variations in the perovskite layer thickness. With its remarkable efficiency, which increases linearly with albedo, the proposed cell can be highly attractive for emerging high-efficiency photovoltaic applications.

***Index Terms*—Albedo, bifacial gain (BG), current-matching, heterojunction with intrinsic thin layer (HIT), optical simulations, perovksite, tandem.**

I. INTRODUCTION

SUSTAINABLE and cost-effective energy generation from environment-friendly sources has been established as one of the biggest global needs in the international energy road map [1]. Photovoltaic technology has become one of the key contributors to world's sustainable energy generation with a rapidly growing market and decreasing costs [2]. While the market-dominant crystalline silicon solar cells [3] have recently demonstrated more than 26% record efficiency [4] approaching closer to the Auger recombination restricted Shockley–Queisser limit of $\sim$29% [5], researchers have been actively pursuing innovations in cell structures and materials that could go beyond the limits of single-junction solar cells while simultaneously minimizing the cost per kW·h. One such approach is to use a tandem cell structure that stacks multiple p-n junctions with higher bandgap materials on top to reduce thermal losses associated with the photoabsorption in the solar spectrum. Efficiencies up to $\sim$35% [6] and 46.5% [7] have been demonstrated with four-junction III–V tandem solar cells without and with light concentration, respectively. While the conventional tandem solar cells have primarily focused on III–V compound materials because of the requirement of lattice matching [8], higher fabrication costs have so far limited their market share for the terrestrial use. Emerging organic/inorganic materials, such as perovskites (PVKs), colloidal quantum dots, nanocrystals, etc., are however not subject to the constraint of lattice matching, which, along with their lower fabrication cost, make them ideally suitable to be integrated with industry standard silicon in a tandem structure. In particular, organic–inorganic mixed lead-halide PVK single-junction cell has recently demonstrated a remarkable efficiency ($\sim$22%), which, in addition to its tunable bandgap (1.5–2.3 eV) and low fabrication cost, makes it a promising candidate to be a top cell in a perovskite/silicon tandem solar cell. A thin layer ($\leq$500 nm [9]) of PVK can be stacked mechanically or monolithically on a silicon solar cell in two-terminal (2-T), 3-T, and 4-T device configurations [10]. Efficiency of $\sim$30% has been forecasted for practical two-junction perovskite/silicon solar cells with 2-T and 4-T device configurations with optimized layer thicknesses and surface texturing [11], whereas the theoretical limits for an ideal bandgap PVK material in a two-junction perovskite/silicon cell approaches to $\sim$41% [12].

In a bid to boost efficiency of two-junction perovskite/silicon tandem cells well above 30%, bifacial solar cells have recently been explored [13]. Bifacial light absorption is one of the effective techniques to enhance the solar cell efficiency through harvesting the reflected (albedo) part of sunlight [14]. Albedo varies for different ground surfaces: maximum is $\sim$90% for snow, whereas the average albedo of earth is $\sim$30% [15].
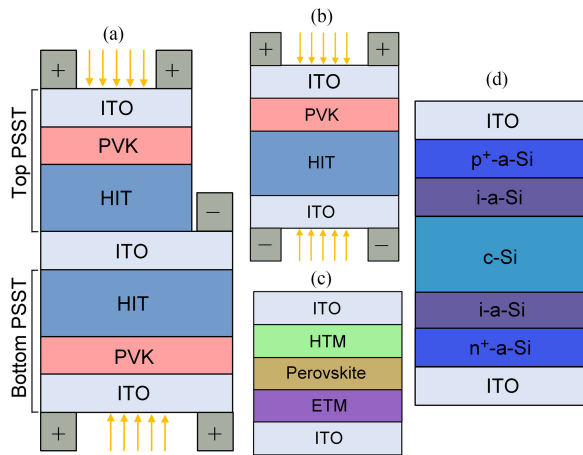
Fig. 1. 2-D schematics of solar cells modeled in this paper. (a) Bifacial perovskite/silicon double-tandem solar cell. (b) Standalone bifacial single-tandem (PSST) solar cell. (c) PVK solar cell. (d) Silicon heterojunction with intrinsic thin layer (HIT) solar cell.

In practice, the bifacial gain (BG) (percentage increase in energy output relative to a monofacial cell) is typically between 10%–30% for various ground surfaces [16] and elevation heights. Although a series-connected two-junction bifacial perovskite/silicon tandem solar cell structure can outperform the bifacial single-junction silicon solar cell, its efficiency gets limited to $\sim 33\%$ even at high albedo ($> 50\%$) [13]. The maximum additional efficiency that could be obtained for this structure at any albedo is limited ($\sim 8\%$) because of the fundamental requirement of current-matching in series-connected tandem solar cells [13]. In this paper, we propose a 3-T, four-junction perovskite/silicon double-tandem (PSDT) solar cell structure that can efficiently harvest light in all ranges of albedo by stacking two tandem perovskite/silicon cells in a flipped configuration with a common (middle) terminal. The BG of this structure is linearly proportional to the rear collection of albedo and does not saturate unlike the series-connected 2-T tandem cell. Using self-consistent device simulations, we establish the quantitative improvements expected from the PSDT cell as compared with standard bifacial silicon solar cells and the two-junction bifacial perovskite/silicon tandem solar cell. In addition, we explore the detailed design space for this cell along with addressing the following key questions: first, what are the optimal material thicknesses for PVK and silicon subcells? and second, what are the potential benefits of the proposed cell at reasonable/practical BGs expected in the field operation?

This paper is divided into five sections. Sections II and III describe the proposed cell structure and modeling approach, respectively. Section IV discusses the results and the conclusions are provided in Section V.

II. Perovskite/Silicon Double-Tandem Cell Structure

A two-dimensional (2–D) schematic diagram of bifacial PSDT solar cell is shown in Fig. 1(a). The cell is implemented by integrating two identical perovskite/silicon single-tandem (PSST) cells monolithically or mechanically in a parallel twin-solar-cell structure. Each of the PSST cells consists of top PVK

subcell connected in series with the bottom HIT subcell with indium-tin-oxide (ITO) layer used as the transparent contact. High-energy photons are absorbed in the PVK subcell because of its higher bandgap, whereas the low-energy photons pass through top cell and get absorbed in the bottom HIT subcell because of its relatively lower bandgap and large thickness. The two PSST cells are connected together via a middle ITO contact forming the third (common) terminal for the parallel configuration. The whole structure forms a bifacial PSDT cell with the top PSST cell facing the direct light, whereas the bottom PSST cell faces the albedo light. It should be noted that although the general concept of series/parallel combination has been proposed before [17], [18] to maximize spectral robustness for tandem cells, the approach used here is uniquely designed to maximize the bifacial performance.

The 2-D schematic of a standalone bifacial PSST cell is shown in Fig. 1(b) with PVK as the top subcell and HIT as the bottom subcell. In this case, albedo is incident on the HIT subcell, which is connected in series with the PVK subcell.

The 2-D schematic of the PVK subcell is shown in Fig. 1(c). PVK is used as photoabsorbing material, whereas hole transport material (HTM) and electron transport material (ETM) are used to realize carrier-selective contacts. We use PCBM as ETM and CuSCN as HTM [19]. For comparison, results are also obtained for PEDOT:PSS as HTM. The 2-D schematic of the HIT subcell is shown in Fig. 1(d). Crystalline silicon (c-Si) is used as photoabsorbing material, whereas thin layers of amorphous silicon (a-Si) are used for carrier-selective contacts at the top and bottom.

III. Modeling Approach

The photoelectrical characteristics of the cell are simulated using a 1-D device simulation tool Automat FOR Simulation of HETero structures (AFORS-HET)[20]. The tool solves the coupled set of cell electrostatics and carrier continuity equations self-consistently. Poisson equation is solved for electrostatics and current transport simulation is implemented using drift-diffusion approximation [21]. The physical parameters for carrier recombination, mobility, and lifetime for cell materials are obtained from published experimental results and are listed in Table I. To account for the intrinsic nonidealities, such as self-shading, we assume that the rear-side collection (R_{rear}) at the cell is two-third of the albedo (R_{A}) in all simulations ($R_{\text{rear}} = \gamma R_{\text{A}}$; $\gamma = 2/3$). With design optimization, such as panel orientation, ground elevation, etc., this value of rear collection has been reported to be practically achievable [16], [22]. In general, we assumed that R_{A} has the same spectrum as that of AM1.5G. Results are also compared by using the real spectrum of various ground surfaces, such as grass, sand etc.

A. Absorption of Solar Spectrum

For the optical modeling of the solar cell, a boundary value problem is solved. A rigorous full-wave method is adopted to find the electromagnetic fields in all the layers of the cell by taking into account all the internal fields arising because of the reflections from the interfaces [23, Sec. 2.3.1.1]. In this method,

TABLE I
PARAMETERS USED FOR SOLAR CELL SIMULATIONS

	PVK subcell			HIT subcell			
	CuSCN	Perovskite	PCBM	p^{++}a–Si	Intrinsic a–Si	c–Si	n^{++}a–Si
Thickness [nm]	40	170	20	10	10	2×10^5	10
ϵ_r	3	6.5	9	11.9	11.9	11.9	11.9
χ [eV]	1.8	3.73	4.17	3.9	3.9	4.05	3.9
E_g [eV]	3.48	1.55	2	1.72	1.72	1.12	1.72
N_c [cm^{-3}]	2.2×10^{18}	2.5×10^{20}	2.2×10^{18}	2.85×10^{19}	2.85×10^{19}	2.85×10^{19}	2.85×10^{19}
N_v [cm^{-3}]	1.8×10^{19}	2.5×10^{20}	1.8×10^{19}	1.04×10^{19}	1.04×10^{19}	1.04×10^{19}	1.04×10^{19}
μ_n [cm^2/V · s]	0.01	40 (20) $\star$	0.01	20	20	1030 (600)$\star$	20
μ_p [cm^2/V · s]	0.01	40 (20)$\star$	0.01	5	5	330 (200)$\star$	5
N_A [cm^{-3}]	3×10^{17}	1×10^{16}	–	5×10^{19}	–	–	–
N_D [cm^{-3}]	–	–	5×10^{17}	–	–	5×10^{15}	5×10^{19}
τ [s]	1×10^{-6}	2×10^{-8}	1×10^{-6}	1×10^{-7}	1×10^{-7}	10^{-2} $(10^{-4})\star$	1×10^{-7}
R_{bb} [cm^3/s]	–	3×10^{-11}	–	1.8×10^{-15}	1.8×10^{-15}	1.1×10^{-14}	1.8×10^{-15}
R_{an} [cm^6/s]	–	1×10^{-29}	–	1.66×10^{-30}	1.66×10^{-30}	1.1×10^{-30}	1.66×10^{-30}
R_{ap} [cm^6/s]	–	1×10^{-29}	–	1.66×10^{-30}	1.66×10^{-30}	3×10^{-31}	1.66×10^{-30}

ϵ_r : Permittivity χ : Electron Affinity E_g : Bandgap $N_c(N_v)$: Density of states $\mu_n(\mu_p)$: Mobility $N_D(N_A)$: Doping τ : Carrier lifetime

R_{bb} : Direct recombination coefficient $R_{an}(R_{ap})$: Auger recombination coefficient $\star$: Values in brackets are for moderated η cells

the solar cell is divided into planar sublayers and the total electric field in each sublayer is written as a sum of waves going into opposite directions with unknown amplitudes. By requiring that the fields satisfy Maxwell equations and the boundary conditions on the interface, the unknown amplitudes of the fields inside each layer are determined using recursive relations in addition to determining total transmission and total reflection amplitude [23, Sec. 2.3.1.1]. For this purpose, a linearly polarized planewave is taken to be normally incident upon the solar cell and each layer is divided into electrically small sublayers of equal thickness that is much smaller than the wavelengths of the incident light. Assuming that the total number of sublayers in the solar cells is N with the nth sublayer bounded by planar interfaces z_{n-1} and z_n, $n \in [1, N]$, $\Delta z = z_n - z_{n-1}$ is the thickness of sublayers, $z_0 = 0$, and z_N is the total thickness of the solar cell, the electric field phasor of the incident planewave can be written as follows:

$$\overline{E}_{inc}(\overline{r}) = a\hat{x}e^{ik_0 z} \tag{1}$$

where a is the incidence amplitude, and $k_0 = \frac{2\pi}{\lambda_0}$ is the free-space wave number. The field phasor of the reflected planewave can be written as follows:

$$\overline{E}_{ref}(\overline{r}) = r\hat{x}e^{-ik_0 z} \tag{2}$$

where r is the reflection amplitude. The field phasor of the transmitted light can be written as follows:

$$\overline{E}_{trans}(\overline{r}) = t\hat{x}e^{ik_0(z-z_N)} \tag{3}$$

where t is the transmission amplitude.

For the computation of total electric field phasor $\overline{E}_n(\overline{r})$ in the nth sublayer, the electric field phasor can be written in terms of upward and downward going waves as follows:

$$\overline{E}_n(\overline{r}) = \overline{E}_n^{up}(\overline{r}) + \overline{E}_n^{dn}(\overline{r}), \quad z_{n-1} < z < z_n, \quad n \in [1, N] \tag{4}$$

where

$$\left. \begin{array}{l} \overline{E}_n^{up}(\overline{r}) = a^{(n)}\hat{x}e^{ik_0 n_n (z-z_{n-1})} \\ \overline{E}_n^{dn}(\overline{r}) = b^{(n)}\hat{x}e^{-ik_0 n_n (z-z_{n-1})} \end{array} \right\} \tag{5}$$

with coefficients $a^{(n)}$ and $b^{(n)}$ to be determined using the recursive method [23, Sec. 2.3.1.1]. The coefficients $a^{(n)}$ and $b^{(n)}$ are the reflected and transmitted amplitudes in each sublayer, respectively. Absorption in each sublayer of the cell can be found by [24]

$$Q_n = k_0 \Delta z \mathrm{Im}(n_n^2) \frac{|\overline{E}_n(z)|^2}{|a|^2}, \quad n \in [1, N] \tag{6}$$

where Im$(\cdot)$ represents the imaginary part, $\Delta z = 0.5$ nm is the spacing between the adjacent sublayers, n_n is the refractive index of the nth sublayer and $E_n(z)$ is the sum of electric fields for the upward and downward going waves in each sublayer.

The total reflectance, total transmittance, and total absorptance of the whole solar cell can be found as follows:

$$R = |r/a|^2 \tag{7}$$

$$T = |t/a|^2 \tag{8}$$

and

$$A = 1 - (R + T) = \sum_{n=1}^{N} Q_n \tag{9}$$

respectively. The last result follows because of the conservation of energy, and was verified by us to validate the optical model
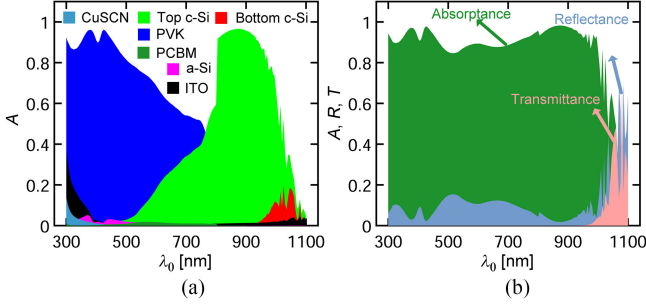
Fig. 2. (a) Absorptance (A) of light incident from top in different layers of the PSDT cell. Photons of shorter wavelength (λ_0) are absorbed in 170-nm top PVK layer because of its high absorption coefficient [25]. The remaining photons are transmitted to the HIT subcell of the top PSST cell where these are partially absorbed in 200-μm c-Si layer. The rest of the lower energy photons are penetrated into the HIT subcell of the bottom PSST cell where most of these get absorbed. (b) Total absorptance (A), reflectance (R), and transmittance (T) of the incident light of the PSDT cell as a function of wavelength (λ_0).
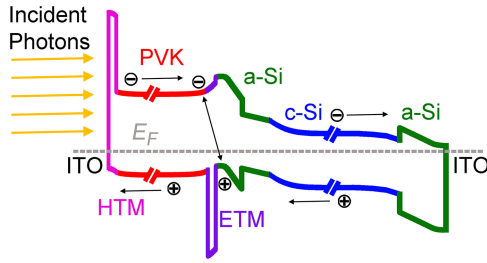

Fig. 3. Energy band diagram of the PSST solar cell under short-circuit condition showing different layers of each subcell. The diagram is not drawn to scale.

by checking that the total absorption of the solar cell computed using (6) is the same as $1 - (R + T)$.

Fig. 2(a) shows the absorptance of different layers of the bifacial PSDT cell as a function of wavelength (λ_0) for PVK thickness (t_{PVK}) of 170 nm and silicon thickness (t_{Si}) of 200 μm. High-energy photons of direct (albedo) sunlight are absorbed in the top (bottom) PVK subcell, whereas most of the low-energy photons are absorbed in silicon of the top (bottom) HIT subcell. A part of low-energy photons is penetrated into the HIT subcell of the bottom (top) PSST cell and absorbed there. Fig. 2(b) shows the total absorptance, reflectance, and transmittance of the PSDT cell as a function of wavelength (λ_0) for $t_{PVK} = 170$ nm and $t_{Si} = 200$ μm.

IV. RESULTS AND DISCUSSION

A. Cell Electrostatics

The energy band diagram of the PSST cell under short-circuit condition is shown in Fig. 3. The light (AM1.5G or albedo) is incident on the PVK subcell and absorbed in both PVK and HIT subcells. The drift-diffusion flux of photogenerated carriers move toward their respective contacts. A perfect recombination interface is considered between the two subcells to allow an ideal series connection for the photocurrent. ITO/a-Si interfaces are considered ohmic, which implies a strong trap-assisted tunneling through the Schottky barriers at these interfaces.
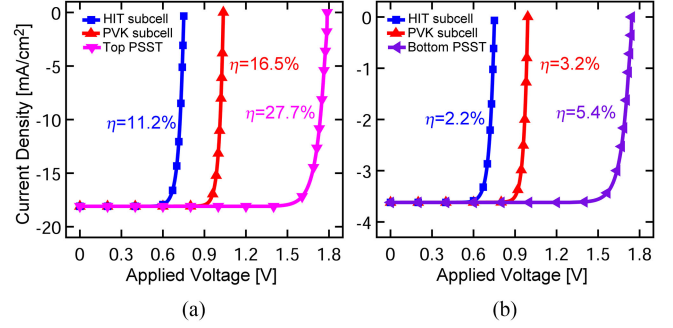

Fig. 4. *J–V* characteristic of (a) top PSST cell and (b) bottom PSST cell along with PVK and HIT subcells for 30% albedo. t_{PVK} and t_{Si} are kept at 170 nm and 200 μm at which $J_{sc,PVK}$ and $J_{sc,HIT}$ are matched and the overall J_{sc} ($J_{sc,PSST}$) remains same because of the series-connected configuration. Note that the efficiency of the bottom PSST cell is calculated with respect to the AM1.5G solar input although it actually receives a lower power intensity mainly because of the bottom albedo incidence.

B. J–V Characteristics of Perovskite/Silicon Single-Tandem and Perovskite/Silicon Double-Tandem Cells

The individual current–voltage (*J–V*) characteristics of top and bottom PSST cells within a bifacial PSDT cell along with their PVK and HIT subcells are shown in Fig. 4(a) and (b), respectively, for 30% albedo. The two subcells within a PSST cell are connected in series, as shown in Fig. 1(b). For the selected subcell thicknesses ($t_{PVK} = 170$ nm, $t_{Si} = 200$ μm), J_{sc} of the PVK subcell ($J_{sc,PVK}$) is matched with that of the HIT subcell ($J_{sc,HIT}$) (see Fig. 6) and the overall J_{sc} ($J_{sc,PSST}$) of the series-connected PSST cell remains the same, whereas V_{oc} adds up. The top PSST cell absorbs most of the direct sunlight and shows an efficiency of 27.7%, with PVK and HIT subcells having 16.5% and 11.2% efficiencies, respectively. The bottom PSST cell, on the other hand, mostly absorbs the albedo ($R_A = 30\%$) and shows an efficiency of 5.4%, with PVK and HIT subcells having 3.2% and 2.2% efficiencies, respectively. It should be noted that the efficiency for the bottom PSST cell is calculated here with respect to the standard AM1.5G.

The *J–V* characteristics of the bifacial PSDT cell along with top and bottom PSST cells are shown in Fig. 5. For the PSDT cell, J_{sc} of both PSST cells adds up while V_{oc} follows the minimum of the two. The bifacial double-tandem solar cell shows 33.1% efficiency for 30% albedo. This is a significant improvement as compared with the single bifacial PSST cell that has an efficiency limit of $\sim$31.5% for all albedos greater than $\sim$30% ([13] and Fig. 7). For higher albedo, the contribution of the bottom PSST cell further increases as we elaborate more in the discussion hereinafter.

C. Effect of Perovskite Thickness

PVK thickness plays an important role in optimizing the cell performance. Here, we show that bifacial PSDT and standalone bifacial PSST cells have their own unique requirements for optimizing t_{PVK} for the best efficiency. For the PSDT cell, the top PSST cell absorbs almost all of the direct sunlight, whereas the bottom PSST cell absorbs almost all of the albedos. Since the incident light on individual PSST cells is monofacial, the
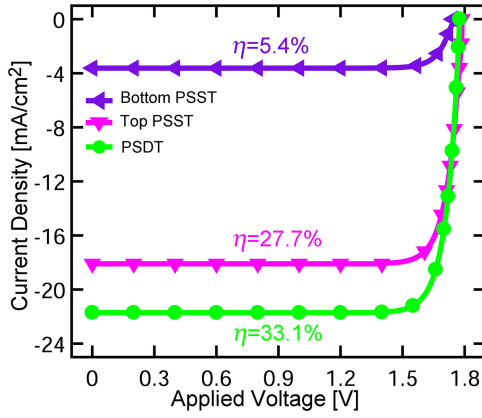
Fig. 5. J–V characteristics of the bifacial PSDT solar cell along with parallel-connected top and bottom PSST solar cells. The bifacial PSDT cell exhibits 33.1% efficiency for 30% albedo (R_A).
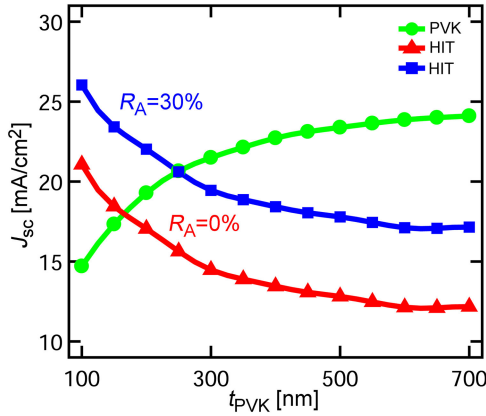

Fig. 7. Efficiency (η) of the standalone bifacial PSST cell as a function of R_A for $t_{Si} = 200$ μm. As albedo is incident to the HIT subcell, R_A mainly affects $J_{sc,HIT}$. η is hence independent of R_A whenever $J_{sc,PSST}$ is limited by $J_{sc,PVK}$.

Fig. 6. Short-circuit current (J_{sc}) in PVK and HIT subcells as a function of PVK thickness (t_{PVK}). Current-matching is achieved at $t_{PVK} = 170$ nm and $t_{PVK} = 250$ nm for $R_A = 0\%$ and $R_A = 30\%$, respectively. The current-matching for $R_A = 0\%$ defines the optimal t_{PVK} for the PSDT cell, whereas for $R_A = 30\%$ defines the optimal t_{PVK} for the standalone bifacial PSST cell.

Fig. 8. Efficiency (η) of the bifacial PSDT cell and the standalone bifacial PSST cell as a function of t_{PVK} for $R_A = 30\%$ and $t_{Si} = 200$ μm. The bifacial PSDT and PSST cells are relatively less sensitive to t_{PVK} as performance of the bifacial PSDT cell decreases by only $\sim 1.2\%$ for ± 25 nm deviation from optimal t_{PVK}, whereas the performance of the bifacial PSST cell decreases by only $\sim 0.9\%$ for ± 25 nm deviation from optimal t_{PVK}. The bifacial PSDT and PSST cells show $\eta = 33.1\%$ and $\eta = 31.5\%$ for $t_{PVK} = 170$ nm and $t_{PVK} = 250$ nm, respectively.

optimization of t_{PVK} for the PSDT cell is therefore similar to that of a monofacial PSST cell that corresponds to $R_A = 0\%$. Fig. 6 shows that how J_{sc} in series-connected subcells of PSST cell are matched by varying t_{PVK} while keeping t_{Si} constant at 200 μm. In the absence of albedo ($R_A = 0\%$), J_{sc} for subcells match at $t_{PVK} \approx 170$ nm, which is hence the optimal t_{PVK} for the PSDT cell. When an individual PSST cell is used as a standalone bifacial cell, t_{PVK} optimization becomes a function of albedo. This is because the albedo is incident directly on the bottom HIT subcell of the PSST cell in the standalone bifacial configuration, which increases J_{sc} of the HIT subcell. The current-matching in the subcells of the PSST cell occurs at a higher t_{PVK} as albedo is increased. For example, Fig. 6 shows that the current-matching occurs at $t_{PVK} = 250$ nm at $R_A = 30\%$. Fig. 7 elaborates the role of R_A for the bifacial PSST cell while varying t_{PVK} and keeping $t_{Si} = 200$ μm. For $t_{PVK} \leq 170$ nm, $J_{sc,PVK} \leq J_{sc,HIT}$, even at $R_A = 0\%$ (see Fig. 6). In this case, increasing R_A (or equivalently, absorption in the HIT subcell) has no effect on η as $J_{sc,PSST}$ remains limited to $J_{sc,PVK}$. As t_{PVK} is increased to 200 nm, $J_{sc,PVK}$ increases and currents in the two subcells now match at $R_A \approx 15\%$, which results in an increase in η relative
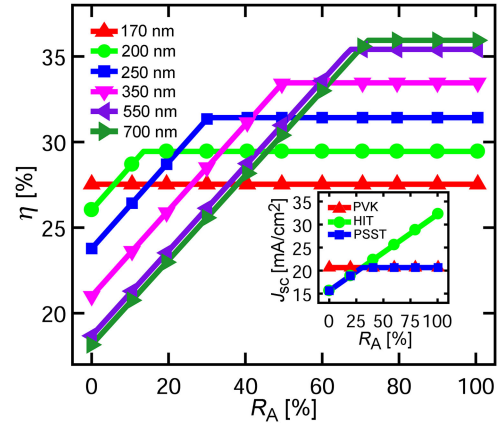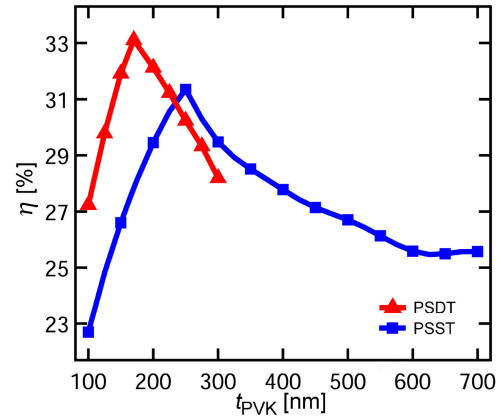
to that of $t_{PVK} = 170$ nm. Further increasing R_A for this case although increases $J_{sc,HIT}$ but $J_{sc,PVK}$ limits the cell current, which makes η independent of R_A. As t_{PVK} is increased up to 250 nm, there is a corresponding increase in $J_{sc,PVK}$ that allows current-matching between the subcells at a higher $R_A \approx 30\%$ (and at a higher current) resulting in an improved η ($\approx 31.5\%$). A similar trend can be seen when t_{PVK} is increased above 250 nm. The maximum η at higher R_A, however, tends to saturate when t_{PVK} is increased to ~ 550 nm. This is consistent with $J_{sc,PVK}$ versus t_{PVK} trend, as shown in Fig. 6, which illustrates a saturating behavior for $t_{PVK} > 550$ nm. The inset of Fig. 7 shows $J_{sc,PSST}$ for $t_{PVK} = 250$ nm and $t_{Si} = 200$ μm as a function of R_A. $J_{sc,PVK}$ is constant but $J_{sc,HIT}$ linearly increases with R_A. Once current-matching is achieved ($R_A \sim 30\%$), $J_{sc,PSST}$ remains limited to $J_{sc,PVK}$ because of series connection.

Fig. 8 compares η of the bifacial PSST (standalone) cell and the bifacial PSDT cell as a function of t_{PVK} for $R_A = 30\%$. The optimal η under this condition for PSST and PSDT solar cells is $\sim 31.5\%$ and 33.1%, respectively, at t_{PVK} of 250 nm
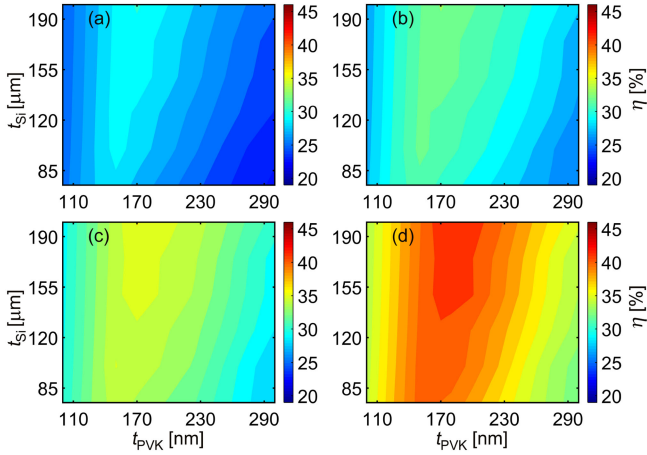
Fig. 9. Combined effect of t_{Si} and t_{PVK} on η of the bifacial PSDT cell. (a) $R_A = 15\%$. (b) $R_A = 30\%$. (c) $R_A = 45\%$. (d) $R_A = 75\%$.

Fig. 10. Efficiency (η) as a function of R_A for different bifacial cells for a constant t_{Si} at 200 μm. The PSDT cell outperforms both HIT and PSST cells with the relative benefit increasing with higher albedo. The inset shows η as a function of R_A for moderate efficiency subcells.

and 170 nm, respectively. The optimal t_{PVK} for the PSST cell corresponds to the current-matching conditions for $R_A \geq 30\%$, as shown in Fig. 6. For the PSDT cell, albedo is mainly absorbed in PVK and HIT subcells of the bottom PSST cell. Optimal t_{PVK} for the PSDT cell is therefore similar to that of a nonbifacial PSST cell (i.e., $R_A = 0\%$), as discussed previously. The η for standard (nonbifacial) tandem perovskite/silicon is reported to be highly sensitive to t_{PVK} (~ 1 mA/cm^2 variation in J_{sc} for deviation of ~ 20 nm in t_{PVK}) [13]. In contrast, Fig. 8 shows that the performance of the bifacial PSDT cell decreases by only $\sim 1.2\%$ for ± 25 nm deviation from optimal t_{PVK}, whereas the performance of the bifacial PSST cell decreases by only $\sim 0.9\%$ for ± 25 nm deviation from optimal t_{PVK}. This advantage of the bifacial PSST cell was also reported in [13].

D. Effect of Silicon Thickness

The combined effect of t_{Si} and t_{PVK} on η of the bifacial PSDT cell is shown in Fig. 9 for $R_A = 15\%-75\%$. For $t_{PVK} \geq 170$ nm, η increases linearly when t_{Si} is increased from 75 to 200 μm at all values of albedo. At $t_{PVK} \geq 170$ nm, current-matching between PVK and HIT subcells occurs at $t_{Si} = 200$ μm. Reducing t_{Si} below 200 μm, therefore, decreases η. For $R_A = 30\%$ and $t_{PVK} = 170$ nm, η is increased from $\sim 30.8\%$ to $\sim 33.1\%$ when t_{Si} is varied form 75 to 200 μm. For $t_{PVK} < 170$ nm, on the other hand, maximum η is achieved for smaller t_{Si}. For this range of t_{PVK}, the current-matching occurs at $t_{Si} < 200$ μm. At a constant t_{Si}, varying t_{PVK} by ± 25 nm around its optimal value changes η by $\sim 1.2\%$. Similar trend can be seen with t_{PVK} and t_{Si} for $R_A > 30\%$, which indicates that an optimal performance can be achieved with the bifacial PSDT cell for a broad range of t_{PVK} even for thinner silicon wafers.

To compare the performance of the proposed bifacial PSDT cell with bifacial HIT and bifacial PSST cells, η as a function of R_A is shown in Fig. 10 keeping $t_{Si} = 200$ μm. Optimal $t_{PVK} = 170$ and 250 nm are chosen for PSDT and PSST cells, respectively. For the bifacial HIT cell, $J_{sc,HIT}$ increases almost linearly with R_A and η reaches $\sim 27.8\%$ for $R_A = 30\%$. On the other hand, η for the bifacial PSST cell first increases with
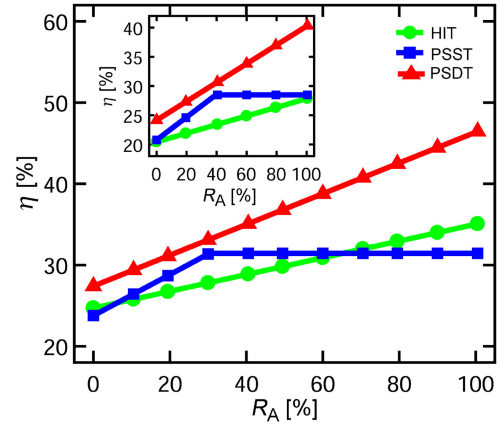
R_A and then saturates at 31.5% as already explained previously in Fig. 7. For the bifacial PSDT cell, η increases almost linearly with R_A for its whole range since the bottom PSST cell keeps adding more current to the PSDT cell with increasing R_A because of the parallel configuration. The bifacial PSDT cell outperforms the bifacial PSST cell for whole range of R_A, reaching the milestone of $\eta \sim 33.1\%$ at around $R_A \approx 30\%$ and exceeding $\eta = 46\%$ for $R_A = 100\%$. BG for the PSDT cell at $R_A = 30\%$ and $R_A = 50\%$ is 20% and 34%, respectively. For the PSST cell, BG is limited to 32% for the same values of R_A. The inset shows η for bifacial HIT, bifacial PSST, and PSDT cells as a function of R_A with moderate efficiency subcells ($\eta_{HIT} = 20.5\%$ and $\eta_{PVK} = 17.5\%$ for standalone cells). The PSDT cell exhibits $\eta \sim 29\%$ for $R_A \approx 30\%$. The cell parameters for moderate efficiency subcells are also given in Table I.

Table II shows the performance of bifacial PSST and PSDT cells simulated using different HTMs and compares these with experimentally reported data in [19]. t_{PVK} is kept constant at 250 nm and the PSST cell is configured in a 4-T configuration. The simulated results for J_{sc} and V_{oc} match remarkably with that of experiment. Fill factor (FF) in simulations is however better as compared with that in experiment possibly because of the effect of nonideal contact resistance in the experimental cells. The experiment and simulations both show that by using CuSCN as HTM in the PVK subcell, efficiencies for PVK and PSST cells are enhanced by $\sim 4\%-6\%$ as compared with that when PEDOT:PSS is used as HTM. With optimized t_{PVK} for $R_A = 30\%$, bifacial PSST and PSDT cells with CuSCN exhibit η of 31.5% and 33.1%, respectively. In comparison, PSST and PSDT cells with PEDOT:PSS exhibit η of 26.4% and 26.8%, respectively.

The performance of bifacial PSST and PSDT cells for albedo spectrum of various ground surfaces is shown in Fig. 11. Maximum albedo is $\sim 95\%$ for snow, whereas albedo of most of the surfaces vary in the range from 20% to 40%. η for bifacial PSST cell saturates at 31.5% for albedo of almost all of the surfaces, whereas η of the bifacial PSDT cell keeps on increasing with albedo. The inset of Fig. 11 compares the η of the PSDT cell as a function of R_A for two cases: R_A has the spectrum identical

TABLE II
PERFORMANCE COMPARISON OF BIFACIAL PSST AND PSDT SOLAR CELLS WITH DIFFERENT HTMS

		$R_A = 0\%$					$R_A = 30\%$	
		$t_{PVK} = 250$ nm					t_{PVK} [Optimal]	
		$J_{sc,PVK}$	$V_{oc,PVK}$	FF_{PVK}	η_{PVK}	η_{PSST} [4–T]	η_{PSST}	η_{PSDT}
		[mA/cm^2]	[V]	[%]	[%]	[%]	[%]	[%]
PVK with PEDOT:PSS	Exp. [19]	18.2	0.90	74.5	12.1	20.9	–	–
PVK with CuSCN	Exp. [19]	21.0	1.1	74.1	17.1	26.7	–	–
PVK with PEDOT:PSS	This Work	18.9	0.92	85.9	14.9	24.6	26.4*	26.8†
PVK with CuSCN	This Work	20.7	1.03	87.7	18.6	28.3	31.5**	33.1††

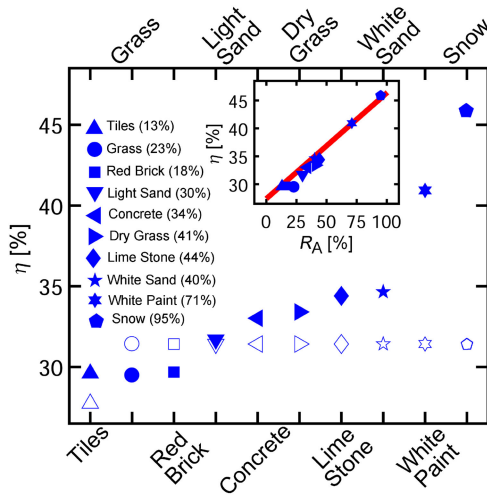*$t_{PVK} = 335$ nm ; **$t_{PVK} = 250$ nm ; †$t_{PVK} = 170$ nm ; ††$t_{PVK} = 170$ nm

Fig. 11. η of standalone bifacial PSST (open symbols) and PSDT (filled symbols) cells for various ground surfaces by using their actual albedo spectrum shown in Fig. 13. The integrated reflectance for each surface with respect to the standard AM1.5G spectrum is also identified. The inset shows η of the bifacial PSDT cell as function of R_A when it is computed using AM1.5G (solid line) and real spectrum of ground albedo (symbols).

to AM1.5G; and R_A has the spectrum calculated using the real spectral reflectance of the ground taking AM1.5G as the incident light. A good match between the two approaches can be observed although the former slightly overestimates η for many surfaces.

It would be interesting to compare the efficiency of our bifacial PSDT cell with that of an ideal bifacial four-junction tandem solar cell. In [30], Alam and Khan have analytically shown that ideal bandgaps for the subcells of a four-junction bifacial tandem cell are in the range 0.85–1.8 eV, capable of providing ∼58% efficiency at $R_A = 30\%$. Although this ideal efficiency is significantly better than that of the simple symmetric structure of the PSDT cell, suitable materials corresponding to the ideal bandgaps and their integration in a solar cell technology are practical challenges that still need to be resolved. Moreover, the loss of light between albedo and rear-side collection has not been considered in [30]. In contrast, the integration of perovskite/silicon tandem cells and mechanical stacking needed in the PSDT cell are relatively simple and has good

prospects to be incorporated in the existing silicon solar cell technologies.

Although the work presented here is focused on the physical/structural aspects of the PSDT cell, we would like to mention that the system level design of bifacial solar cells is also very important. In particular, special consideration associated with the ratio of diffuse/global irradiance, optimization of tilt angle, elevation, and self-shading, etc., needs to be properly addressed at the system level [31], [32].

V. CONCLUSION

We have proposed and investigated an innovative 3-T, four-junction bifacial tandem solar cell structure that can effectively leverage albedo to boost efficiency above the current-matching limits of the conventional structures. The proposed cell stacks two perovskite/silicon tandem solar cells by joining their HIT subcells through an intermediate transparent conducting oxide. A parallel connection between the two tandem cells enables the bottom cell to contribute effectively to the overall current by harvesting the albedo. The cell shows a steady efficiency for a broad range of silicon thickness performing best at around 200 μm with efficiency approaching 33.1% for average earth's albedo of 30% assuming rear-side collection of almost two-third of the albedo. PVK thickness needs to be carefully designed to get an optimal current-matching within the subcells. Unlike series-connected 2-T tandem cells, the optimal top cell thickness is independent of the value of albedo and the BG does not saturate (increases linearly) with increasing albedo. In contrast with the conventional perovskite/silicon tandem cells, the proposed cell is relatively less sensitive to PVK thickness as performance decreases by only ∼1.2% for ±25 nm deviation from the optimal thickness. Although the fabrication of a PSDT cell is expected to be more expensive as compared with standard two-junction perovskite/silicon tandem cells, the increased energy output is likely to offset the increase in cost. The cell therefore exhibits a promising potential for the locations having modest to high values of albedo.

APPENDIX

Fig. 12 shows the refractive indices (n) and extinction coefficients (k) of materials used in this paper [19], [20],
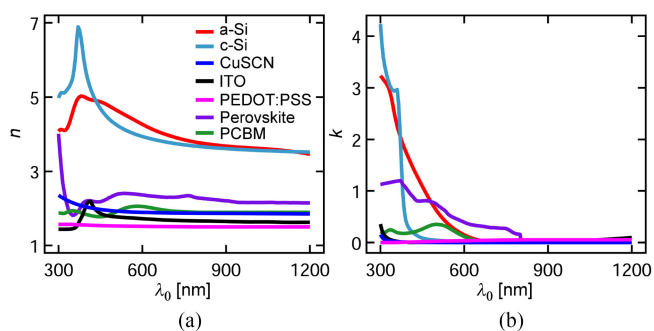
Fig. 12.   Refractive indices (*n*) and extinction coefficients (*k*) of materials used in this paper [19], [20], [26]–[29].
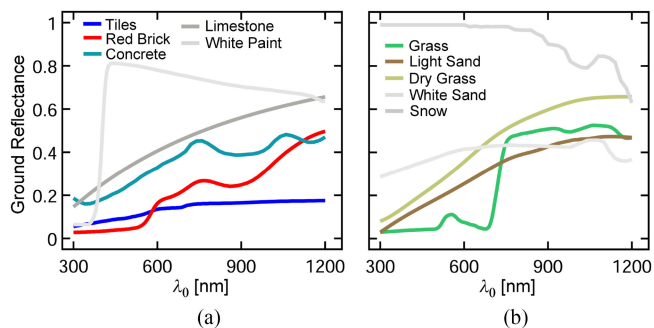

Fig. 13.   Albedo of different ground surfaces [33]–[36].

[26]–[29]. Albedo of different ground surfaces [33]–[36] is shown in Fig. 13.

REFERENCES

[1] N. Panwar, S. Kaushik, and S. Kothari, "Role of renewable energy sources in environmental protection: A review," *Renewable Sustain. Energy Rev.*, vol. 15, no. 3, pp. 1513–1524, 2011.

[2] A. Akella, R. Saini, and M. P. Sharma, "Social, economical and environmental impacts of renewable energy systems," *Renewable Energy*, vol. 34, no. 2, pp. 390–396, 2009.

[3] M. Fischer, A. Metz, and S. Raithel, "Semi international technology roadmap for photovoltaics (ITRPV) challenges in c-Si technology for suppliers and manufacturers," in *Proc. Eur. Photovolt. Sol. Energy Conf. Exhib.*, 2012, pp. 527–532.

[4] K. Yoshikawa *et al.*, "Silicon heterojunction solar cell with interdigitated back contacts for a photoconversion efficiency over 26%," *Nature Energy*, vol. 2, 2017, Art. no. 17032.

[5] A. Polman, M. Knight, E. C. Garnett, B. Ehrler, and W. C. Sinke, "Photovoltaic materials: Present efficiencies and future challenges," *Science*, vol. 352, no. 6283, 2016, Art. no. aad4424.

[6] F. Dimroth *et al.*, "Wafer bonded four-junction GaInP/GaAs//GaInAsP/GaInAs concentrator solar cells with 44.7% efficiency," *Prog. Photovolt.*, vol. 22, no. 3, pp. 277–282, 2014.

[7] T. N. Tibbits *et al.*, "New efficiency frontiers with wafer-bonded multi-junction solar cells," in *Proc. 29th Eur. Photovolt. Sol. Energy Conf. Exhib.*, 2014, pp. 1–4.

[8] R. Lachaume *et al.*, "Detailed analysis of III-V/epi-SiGe tandem solar cell performance including light trapping schemes," *Sol. Energy Mater. Sol. Cells*, vol. 166, pp. 276–285, 2017.

[9] H. J. Snaith, "Perovskites: The emergence of a new era for low-cost, high-efficiency solar cells," *J. Phys. Chem. Lett.*, vol. 4, no. 21, pp. 3623–3630, 2013.

[10] C. D. Bailie *et al.*, "Mechanically stacked and monolithically integrated perovskite/silicon tandems and the challenges for high efficiency," in *Proc. IEEE 42nd Photovolt. Spec. Conf.*, 2015, pp. 1–3.

[11] M. Filipič *et al.*, "CH$_3$NH$_3$PbI$_3$ perovskite/silicon tandem solar cells: Characterization based optical simulations," *Opt. Express*, vol. 23, no. 7, pp. A263–A278, 2015.

[12] M. H. Futscher and B. Ehrler, "Efficiency limit of perovskite/Si tandem solar cells," *ACS Energy Lett.*, vol. 1, no. 4, pp. 863–868, 2016.

[13] R. Asadpour, R. V. Chavali, M. R. Khan, and M. A. Alam, "Bifacial Si heterojunction-perovskite organic-inorganic tandem to produce highly efficient solar cell," *Appl. Phys. Lett.*, vol. 106, no. 24, 2015, Art. no. 243902.

[14] A. Cuevas, "The early history of bifacial solar cells," in *proc. 20th Eur. Photovolt. Sol. Energy Conf. Exhib.*, 2005, pp. 801–805.

[15] P. Goode *et al.*, "Earthshine observations of the earth's reflectance," *Geophys. Res. Lett.*, vol. 28, no. 9, pp. 1671–1674, 2001.

[16] B. Zhao, X. Sun, M. R. Khan, and M. A. Alam, "Purdue university bifacial module calculator (PUB)," Feb. 2018. [Online]. Available: https://nanohub.org/resources/pub

[17] T. Trupke and P. Würfel, "Improved spectral robustness of triple tandem solar cells by combined series/parallel interconnection," *J. Appl. Phys.*, vol. 96, no. 4, pp. 2347–2351, 2004.

[18] J. C. Jimeno *et al.*, "Upgrading the silicon IBC to the 40% efficiency," in *Proc. IEEE 43rd Photovolt. Spec. Conf.*, 2016, pp. 0651–0656.

[19] C. O. Ramirez Quiroz *et al.*, "Balancing electrical and optical losses for efficient 4-terminal Si-perovskite solar cells with solution processed percolation electrodes," *J. Mater. Chem. A*, vol. 6, pp. 3583–3592, 2018.

[20] R. Varache *et al.*, "Investigation of selective junctions using a newly developed tunnel current model for solar cell applications," *Sol. Energy Mater. Sol. Cells*, vol. 141, pp. 14–23, 2015.

[21] R. F. Pierret, *Advanced Semiconductor Fundamentals*, vol. 6. Upper Saddle River, NJ, USA: Prentice-Hall, 2003.

[22] C. Reise and A. Schmid, "Realistic yield expectations for bifacial PV systems—An assessment of announced, predicted and observed benefits," in *Proc. 31st Eur. Photovolt. Sol. Energy Conf. Exhib.*, Hamburg, Germany, 2015, pp. 1775–1779.

[23] J. Polo, T. Mackay, and A. Lakhtakia, *Electromagnetic Surface Waves: A Modern Perspective*. Amsterdam, The Netherlands: Elsevier, 2013.

[24] M. V. Shuba, M. Faryad, M. E. Solano, P. B. Monk, and A. Lakhtakia, "Adequacy of the rigorous coupled-wave approach for thin-film silicon solar cells with periodically corrugated metallic backreflectors: Spectral analysis," *J. Opt. Soc. Amer. A*, vol. 32, no. 7, pp. 1222–1230, 2015.

[25] Y. Li *et al.*, "Direct observation of long electron-hole diffusion distance in CH$_3$NH$_3$PbI$_3$ perovskite thin film," *Sci. Rep.*, vol. 5, 2015, Art. no. 14485.

[26] H. Shen and B. Maes, "Combined plasmonic gratings in organic solar cells," *Opt. Express*, vol. 19, no. 106, pp. A1202–A1210, 2011.

[27] A. Lenz, H. Kariis, A. Pohl, P. Persson, and L. Ojamäe, "The electronic structure and reflectivity of PEDOT: PSS from density functional theory," *Chem. Phys.*, vol. 384, no. 1–3, pp. 44–51, 2011.

[28] G. Xing *et al.*, "Low-temperature solution-processed wavelength-tunable perovskites for lasing," *Nat. Mater.*, vol. 13, no. 5, pp. 476–480, 2014.

[29] M. A. Green, "Self-consistent optical parameters of intrinsic silicon at 300 K including temperature coefficients," *Sol. Energy Mater. Sol. Cells*, vol. 92, no. 11, pp. 1305–1310, 2008.

[30] M. A. Alam and M. R. Khan, "Thermodynamic efficiency limits of classical and bifacial multi-junction tandem solar cells: An analytical approach," *Appl. Phys. Lett.*, vol. 109, no. 17, 2016, Art. no. 173504.

[31] U. A. Yusufoglu *et al.*, "Analysis of the annual performance of bifacial modules and optimization methods," *IEEE J. Photovolt.*, vol. 5, no. 1, pp. 320–328, Jan. 2015.

[32] J. P. Singh, T. M. Walsh, and A. G. Aberle, "Performance investigation of bifacial PV modules in the tropics," in *Proc. 27th Eur. Photovolt. Sol. Conf. Exhib.*, 2012, pp. 3263–3266.

[33] C. Gueymard, *SMARTS2: A Simple Model of the Atmospheric Radiative Transfer of Sunshine: Algorithms and Performance Assessment*. Cocoa, FL, USA: Florida Sol. Energy Center, 1995.

[34] M. Wendisch *et al.*, "Airborne measurements of areal spectral surface albedo over different sea and land surfaces," *J. Geophys. Res.*, vol. 109, no. D8, 2004.

[35] J. Turner, A. Parisi, and D. Turnbull, "Reflected solar radiation from horizontal, vertical and inclined surfaces: Ultraviolet and visible spectral and broadband behaviour due to solar zenith angle, orientation and surface type," *J. Photochem. Photobiol.*, vol. 92, no. 1, pp. 29–37, 2008.

[36] T. Zinner *et al.*, "Ground-based imaging remote sensing of ice clouds: Uncertainties caused by sensor, method and atmosphere," *Atmos. Meas. Techn.*, vol. 9, no. 9, pp. 4615–4632, 2016.

Authors' photographs and biographies not available at the time of publication.